Highly Nonlinear Wave Propagation in Elastic Woodpile Periodic Structures

E. Kim,[1] F. Li,[1] C. Chong,[2] G. Theocharis,[3] J. Yang,[1] and P.G. Kevrekidis[2]

[1]*Aeronautics and Astronautics, University of Washington, Seattle, WA 98195-2400*
[2]*Department of Mathematics and Statistics, University of Massachusetts, Amherst MA 01003-4515, USA*
[3]*Laboratoire d' Acoustique de l' Université du Maine, UMR-CNRS, 6613 Avenue Olivier Messiaen, 72085 Le Mans, France*

(Dated: November 27, 2014)

In the present work, we experimentally implement, numerically compute with and theoretically analyze a configuration in the form of a single column woodpile periodic structure. Our main finding is that a Hertzian, locally-resonant, woodpile lattice offers a test bed for the formation of genuinely traveling waves composed of a strongly-localized solitary wave on top of a small amplitude oscillatory tail. This type of wave, called a *nanopteron*, is not only motivated theoretically and numerically, but are also visualized experimentally by means of a laser Doppler vibrometer. This system can also be useful for manipulating stress waves at will, for example, to achieve strong attenuation and modulation of high-amplitude impacts without relying on damping in the system.

PACS numbers: 45.70.-n 05.45.-a 46.40.Cd

arXiv:1411.7062v1 [cond-mat.other] 25 Nov 2014

Introduction. Granular crystals are rapidly becoming a popular vehicle for the theoretical study, numerical exploration and experimental identification of a wide range of phenomena ranging from the near linear, to the weakly or even highly nonlinear limit [1–4]. The relevant chains consist of assemblies of particles in one-, two- and three-dimensions inside a matrix (or a holder) in ordered, closely packed configurations. An especially appealing characteristic of such structures is the ability to tune their dynamic response by an applied static load. This may place the system in a near linear or weakly nonlinear regime, in the case of precompressed chains, or even in a highly nonlinear regime, in the absence of such static load (often termed sonic vacuum, due to the vanishing sound speed in that case) [1]. It is exactly this dynamic tunability and the controllability of both the assembly and the measurement of these settings that has enabled a wide range of proposals for applications. Among others, we note shock and energy absorbing layers [5–7], acoustic lenses [8], acoustic diodes [9], and sound scramblers [10].

While various geometries of building blocks have been reported (e.g., spherical, toroidal, or elliptical shapes), granular crystals in woodpile architectures, made of orthogonally stacked rods, are largely unexplored. This is in contrast to their electromagnetic counterpart – called woodpile *photonic* crystals – that successfully demonstrated their efficacy and versatility in manipulating electromagnetic waves [11, 12]. Even existing studies on woodpile *phononic* crystals are limited primarily to their linear elastic responses [13–15], without addressing their nonlinear wave dynamics.

In this Letter, we show that periodic structures in woodpile configurations can be very useful in manipulating highly nonlinear stress waves at will, including high wave attenuation and spontaneous formation of novel traveling waves after an impact excitation. Arguably, the most fundamental waveform that arises in granular chains within the sonic vacuum is a solitary wave with a highly localized waveform [16–21]. Recently, other types of coherent traveling waves in granular chains, within the sonic vacuum, were predicted to exist; periodic traveling waves [19, 22] and static or traveling breathers in granular chains including on-site potentials [23].

Here, we report experimental evidence of the existence of a new type of nonlocal solitary wave within the sonic vacuum. It consists of a highly localized solitary waveform on top of an extended, small-amplitude periodic tail, existing in granular chains with local resonators. Such a solution, satisfying all the other requirements of a solitary wave except that it asymptotes not to zero but to a small amplitude oscillation at infinity, has been long termed a *nanopteron* [24]. This nanopteron arises in numerous models including continuum [25–27] and discrete [28] dynamical systems. Some examples, like the ϕ^4 breather, have received considerable theoretical attention [25, 29, 30] and relevant reviews/books have summarized much of this *nonlocal solitary wave* activity [31, 32]. Nevertheless, experimental studies of the nanopteron are extremely limited [27].

In what follows, we present the experimental setup of the woodpile lattice and a brief overview of its description via an effective discrete element model (DEM). In different regimes, we experimentally observe (i) the spontaneous formation and steady propagation of the nanopteron, (ii) the potential breathing of the solitary waves, i.e., modulation as they travel or (iii) the decay of the solitary waves, which is due to the coupling to the resonators, rather than the damping of the system. All of the relevant features are corroborated by numerical computations, and some of the salient features are explained theoretically. We thus believe that this study provides a roadmap for further exploration and analysis of highly nonlinear waves in a host of settings, including most notably granular chain models with the addition of

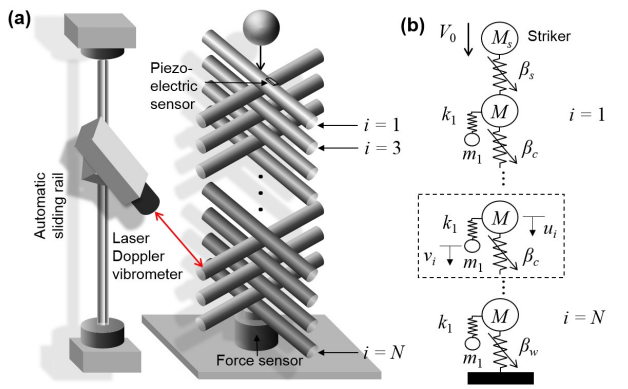

FIG. 1: Schematic of (a) experimental setup and (b) discrete element model; see text for details.

an *internal resonator* on each node, a context that has recently been of considerable interest in its own right [33–37].

Experimental and Theoretical Setup. Figure 1 illustrates the experimental setup of our 1D woodpile structure and the corresponding DEM. The chain is composed of orthogonally stacked cylindrical rods made of fused quartz (Young's modulus $E = 72$ GPa, Poisson's ratio $v = 0.17$, and density $\rho = 2200$ kg/m^3). We test three different rod lengths: [20, 40, 80] mm, while keeping their diameters identical to 5.0 mm. We excite the chain by striking the center of the uppermost rod with a 10 mm-diameter glass sphere. While we present in this Letter the results for a measured impact velocity of $V_0 = 1.97$ m/s, the effect of varying striker velocities can be found in the supplemental document. We record the transmitted stress waves using a piezoelectric force sensor (PCB C02) placed at the bottom of the woodpile chain. To investigate the propagating waveforms along the path, we alter the number of stacked cylinders from one to N (total number of cylinders) and synchronize the signals with respect to the striker impact moment, which is detected by a small piezoelectric ceramic plate bonded on the surface of the top rod. A particular challenge within our setup concerns the experimental identification of the especially weak oscillations of the unit cells that are critical for our reported observation of the nanopteron. For this, we introduce a laser Doppler vibrometer (Polytec, OFV-505), which is mounted on an automatic sliding rail to detect localized vibrations of each rod in the resolution of 0.02 μm/s/Hz$^{1/2}$.

As suggested by Fig. 1(b), the dynamics of the woodpile lattice along the axis of the contacts can be effectively described by a system of nonlinear oscillators that are coupled to adjacent masses. Assuming the principal nodes (associated with the rods' axial motion) as having mass M and a coupling of β_c, and the internal resonators within the rods as having a coupling of k_1 and a mass of

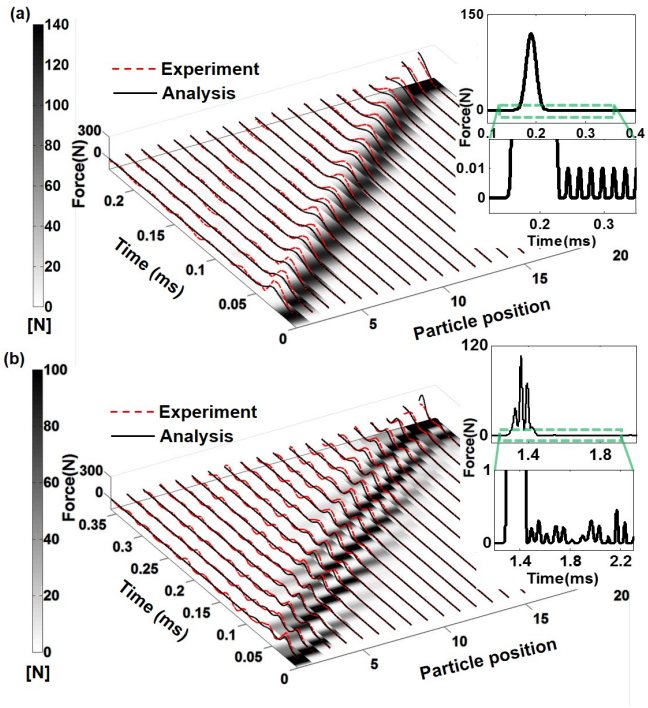

FIG. 2: Numerical (solid black) and experimental (dashed red) force profiles in space-time (measured in ms) in 1D woodpile crystals composed of (a) 20 mm and (b) 40 mm rods. The insets show the numerical magnified force profiles of nanoptera, while the colormap represents the magnitude of the contact force.

m_1, we propose the following generalized Hertzian DEM,

$$M\ddot{u}_i = \beta(u_{i-1} - u_i)^{3/2} - \beta(u_i - u_{i+1})^{3/2} + k_1(v_i - u_i), \quad (1)$$

$$m_1\ddot{v}_i = k_1(u_i - v_i). \quad (2)$$

This model allows us to describe longitudinal excitations along the axis of the contacts in the presence of internal vibration modes that can store energy in their own right.

The effective parameters m_1, M and k_1 of this DEM description are determined via an optimization process based on the envelopes of propagating waves (see the supplemental material for further details). Note that in Eq. (1), β assumes the value β_c within the chain, while it is β_s for the coupling of the striker to the first bead and β_w for the coupling of the last bead to the wall (cf. Fig. 1). In what follows, we will rescale the time $t \to t\sqrt{\beta_c/M}$ and the coupling $\kappa = k_1/\beta_c$ for the purposes of our analysis. The mass ratio is denoted as $\nu = m_1/M$.

Experimental Observations, Numerical Corroboration and Theoretical Analysis. Figures 2(a) and (b) illustrate the comparison of the wave propagation in 1D woodpile lattices composed of 20 particles of 20 mm and 40 mm rods respectively. Dashed red (solid black) curves represent the contact force profiles obtained by experiments (numerics). The numerical results are also shown

in the underlying surface maps to ease visualization of wave modulation effects. In addition to the accurate representation of the experimental findings by the DEM, we can make a few further observations here. In the case of 20 mm rods, the striker rapidly settles into a solitary wave (in a way reminiscent of the standard granular chain [1, 2] – however with a significant difference, as we will see below). For the 40 mm case, a traveling breather appears to form in a pattern similar to numerical observations in [23]. This wave emerges after a transient period in which a primary wave experiences an exponential decay (which can be computed semi-analytically; see supplemental material) and a secondary wave emerges due to the coupling with the resonators. However, a key feature shared by *both* traveling structures is the existence of a persistent form of background oscillation as seen in the insets of Fig. 2. We note that here the wake of the principal pulse has a constant amplitude tail. This feature which has also been confirmed by means of simulations in considerably larger chains (not shown here) is different from what is the case in the so-called Kawahara solitary waves, where the tail is decaying in amplitude away from the main wave shape [38]. We now explore this *nanopteronic* waveform more quantitatively.

The surface maps in Fig. 3(a) and (b) show the analytical and experimental velocity profiles respectively of the tails of the observed waveforms that appear in a 40 particle chain of 20 mm rods. The traveling waves spontaneously become nanoptera by developing oscillatory patterns of velocity, which clearly follow the principal solitary wave (highlighted in red color). It should be noted that the velocities involved in the nanopteronic tails are approximately three orders of magnitude smaller than those of the solitary waves; yet, they can be accurately measured through our laser Doppler vibrometer. The frequency and wavenumber content of the nanopteronic tail can be obtained by conducting the fast Fourier transform (FFT) in time- and space-domains (shown in Fig. 3(c) and (d)). The resonant frequency of the experimental data shown in panel (c) is 54.93 kHz, which is found to be directly connected to the relative motion of the two masses (the primary and the resonator ones), namely $\omega_0 = \sqrt{\kappa(1+1/\nu)}$ (55.45 kHz according to the DEM). For a traveling wave of speed c, the corresponding wavenumber in panel (d) is found to satisfy the relation $\omega_0 = ck_0$. In Fig. 3(d), we obtain $k_0 = 119$ m^{-1} experimentally, which is in agreement with the value $k_0 = 120$ m^{-1} obtained via the DEM (see the supplemental document for details).

We now theoretically justify this feature, namely the existence of the relative motion between the primary node and the resonator, in the nanopteronic tail of the observed wave structure. Setting up the so-called strains of the two fields $r_i = u_{i-1} - u_i$ and $s_i = v_{i-1} - v_i$, seeking traveling waves therein as $r_i(t) = R(i - ct) = R(\xi)$, $s_i = S(i - ct) = S(\xi)$ and then using the Fourier transform $R(\xi) = \int_{-\infty}^{\infty} \hat{R}(k)e^{ik\xi}dk$ (and similarly for S), leads from Eqs. (1)-(2) to

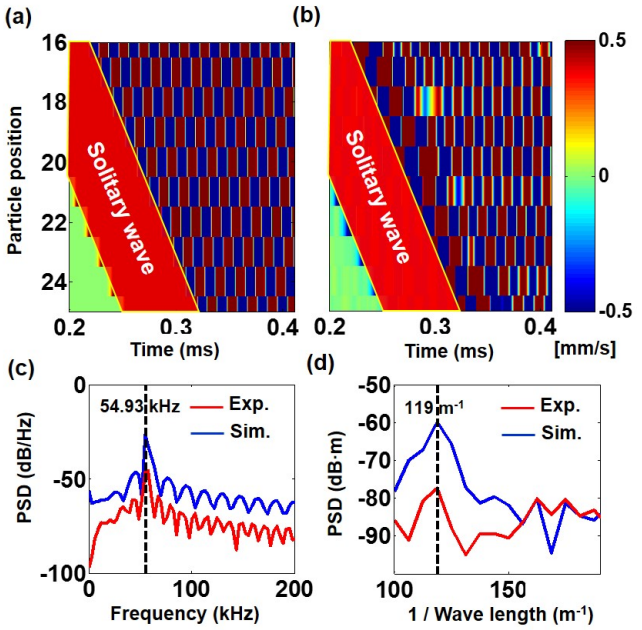

FIG. 3: (a) Numerical and (b) experimental velocity profiles of nanoptera formed in a 40 particle chain of 20 mm rods. (c) Frequency and (d) wave number contents of the tail constructed by FFT of velocity profiles in specific time- and space-domains, respectively (particle spot $i = 24$ and time $t = 0.4$ ms).

$$\hat{R} = \frac{1}{c^2}\mathrm{sinc}^2\left(\frac{k}{2}\right)\widehat{R^{3/2}} + \frac{\kappa}{k^2c^2}(\hat{R} - \hat{S}), \quad (3)$$

$$\hat{S} = \frac{\kappa}{\kappa - c^2k^2\nu}\hat{R}. \quad (4)$$

Substituting Eq. (4) into Eq. (3) and reshaping the relevant expression yields

$$\hat{R} = \left[\frac{1}{c^2}\mathrm{sinc}^2\left(\frac{k}{2}\right) + \frac{1}{c^4}\frac{\kappa}{k^2 - k_0^2}\mathrm{sinc}^2\left(\frac{k}{2}\right)\right]\widehat{R^{3/2}}. \quad (5)$$

Recall that $\mathrm{sinc}(x) = \sin(x)/x$. Invoking the convolution theorem leads us to write

$$R(x) = K * R^{3/2} = \int_{-\infty}^{\infty} K(x-y)R^{3/2}(y)dy, \quad (6)$$

where $K(x) = \Lambda(x) + M(x)$, where $\Lambda(x) = (1/c^2)\max(1-|x|, 0)$ and appears in the corresponding calculation for the granular chain without internal resonators [18]. For $M(x)$ we find

$$(2c^4k_0^3/\kappa)M(x) = |1-x|(\mathrm{sinc}(k_0(1-x)) - k_0) \quad (7)$$
$$-2|x|(\mathrm{sinc}(k_0x) - k_0) + |x+1|(\mathrm{sinc}(k_0(x+1)) - k_0).$$

Thus, the sinusoidal dependence with the periodicity dictated by k_0 within $M(x)$ is directly responsible for the

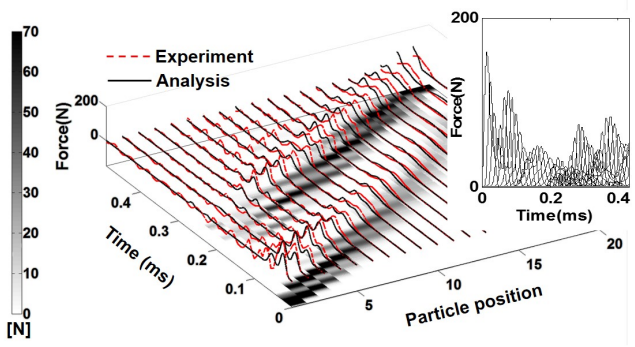

FIG. 4: Experimental and numerical space-time wave modulation results in woodpile woodpile crystals composed of 80 mm rods.

formation of the nanopteronic tails; cf. also the resonant term in the Fourier space expression of Eq. (5). In the granular chain without the resonators, the presence of solely the Λ term in Eq. (5) produces a monotonically decaying solitary wave according to a double exponential law [18, 20]. Here, the presence of the sinusoidal terms within $M(x)$ justifies the form of the nanopteron, where the localized central wave is supported against the backdrop of linear relative vibrations between each node and its corresponding resonator.

Finally, it should be noted that the present setup provides numerous additional opportunities for a wide range of studies within this class of models. One such consists of modifying the rod length. For example, the experimental and numerical results for 80 mm rods is shown in Fig. 4. In this case, the DEM needs to account for two internal resonant modes within the rod and hence two resonators (v_i, w_i) are attached to each principal node of the chain (u_i). As a result, we observe that in this case, the large-amplitude striker impact drastically decays through an effective excitation of the internal resonant modes which disperse the energy in both the temporal and the spatial domain. The inset of Fig. 4 depicts the overlapped profiles of nonlinear waves obtained from various particle positions, which evidently indicate the decaying trend of the propagating waves due to the coupling to the resonators. This wave attenuation suggests that the woodpile periodic structure could be used as an efficient impact mitigator without relying on damping in the system. We should note here that although in this exposition we have highlighted some of the salient features of the model, numerous additional details including the experimental setup, the precise selection of the DEM parameters and the quantitative nature of the agreement between theory, numerics and experiment are provided in the supplemental material (see e.g. Fig. 8 therein).

Conclusions and Future Challenges. In the present work, we have offered a prototypical example of a woodpile granular crystal, consisting of a chain of orthogonally stacked cylindrical rods. In addition to developing the experimental techniques enabling a distributed space-time sensing of the chain, we have provided a theoretical discrete element model that captures the fundamental experimental characteristics of the system, while generalizing the standard Hertzian chain via the inclusion of at least one or modularly more on-site resonators. We have seen that this inclusion provides the possibility for a potential breathing traveling wave or even decay of the initial strong impulse. More importantly, the relative motion between each node and the attached resonator provides the linear mode which constitutes the background for the formation of a weakly nonlocal solitary wave, i.e., a nanopteron. Despite the small magnitude of the tails of the nanoptera (differing by three orders of magnitude with respect to the principal wave), we were able to experimentally observe and compute these tails and to theoretically account for the wavenumber/frequency of their periodicity.

This study leads to a number of topics for potential future work. From a rigorous mathematical perspective, proving the existence of the nanopteron provides a novel set of challenges. At the discrete element model level, quantifying the properties of the system in the case of one or more resonators by detailing the interplay between principal and secondary waves or the role of parametric variations (such as tuning the resonant frequency of the coupling between unit cells etc.) would be of particular interest. It is also relevant to point out that our numerically/experimentally observed nanoptera have a tail only on one side (i.e., are "one-sided" nanoptera), while the typical examples previously known have tails on both sides. Understanding when one-sided vs. two-sided installments of such coherent structures may arise could be of particular interest for future work. In the same vein, considering the results of collisions of two such (e.g. counter-propagating) waves could also shed light on the robustness of such one-sided nanoptera, as well as potentially lead to the formation of two-sided variants thereof. Finally, several questions naturally emerge in experimental investigations. This includes examining the problem in the presence of precompression and its generalization to higher order settings. From a practical perspective, this woodpile structure can offer a new way to modulate, localize, or mitigate external impacts for engineering devices and associated applications.

Acknowledgements. We thank C. Daraio, D. Khatri and D. Frantzeskakis for helpful discussions. JK and PGK acknowledge the support of NSF (CMMI-1414748, CMMI-1000337, DMS-1312856), AFOSR (FA9550-12-1-0332) and ONR (N000141410388). GT aknowledges financial support from FP7-CIG (Project 618322 ComGranSol).

[1] V.F. Nesterenko, Dynamics of Heterogeneous Materials, Chapter 1, Springer-Verlag (New York, 2001).

[2] S. Sen, J. Hong, J. Bang, E. Avalosa, R. Doney, Physics Reports **462**, 21-66 (2008).

[3] P.G. Kevrekidis, IMA J. Appl. Math. **76**, 389 (2011).

[4] G. Theocharis, N. Boechler, and C. Daraio, in *Phononic Crystals and Metamaterials*, Ch. 6, Springer Verlag, (New York, 2013)

[5] C. Daraio, V. F. Nesterenko, E. B. Herbold, and S. Jin, Phys. Rev. Lett. **96**, 058002 (2006).

[6] J. Hong, Phys. Rev. Lett. **94**, 108001 (2005).

[7] R. Doney and S. Sen, Phys. Rev. Lett. **97**, 155502 (2006).

[8] A. Spadoni and C. Daraio, Proc Natl Acad Sci USA, **107**, 7230, (2010).

[9] N. Boechler, G. Theocharis, C. Daraio, Nature Materials **10**, 665 (2011).

[10] V. F. Nesterenko, C. Daraio, E. B. Herbold, and S. Jin, Phys. Rev. Lett. **95**, 158702 (2005).

[11] A. Feigel et al., Appl. Phys. Lett. **83**, 4480 (2003).

[12] H. Liu, J. Yao, D. Xu, and P. Wang, Optics Express. **15**:2, 695 (2007).

[13] H. Jiang, Y. Wang, M. Zhang, Y. Hu, D. Lan, Y. Zhang, and B. Wei, Appl. Phys. Lett. **95**, 104101 (2009).

[14] L.Y. Wu and L.W. Chen, J. Phys. D: Appl. Phys. **44**, 045402 (2011).

[15] E. Kim and J. Yang, J. Mech. Phys. Solids **71**, 33 (2014).

[16] V.F. Nesterenko, J. Appl. Mech. Techn. Phys. **24**, 733 (1983).

[17] R.S. MacKay, Phys. Lett. A **251**, 191 (1999).

[18] J. M. English and R. L. Pego, Proceedings of the AMS **133**, 1763 (2005).

[19] Y. Starosvetsky and A.F. Vakakis, Phys. Rev. E **82**, 026603 (2010).

[20] A. Stefanov and P. Kevrekidis, Nonlinearity **26**, 539 (2013).

[21] A. Chaterjee, Phys. Rev. E **59**, 5912 (1999).

[22] G. James, J. Nonlinear Sci. **22** 813 (2012).

[23] G. James, P.G. Kevrekidis and J. Cuevas, Phys. D **251**, 39 (2013).

[24] J.P. Boyd, "Weakly non-local solitary waves" pp. 51-97 in Nonlinear Topics in Ocean Physics: Proceedings of the Fermi School, A.R. Osborne and L. Bergamasco Eds. (Amsterdam: North-Holland, 1991)

[25] M. Kruskal, H. Segur, Phys. Rev. Lett. **58**, 747 (1987).

[26] A.V. Buryak, Phys. Rev. E **52**, 1156 (1995); N.N. Akhmediev, A.V. Buryak, Opt. Commun. **121**, 109 (1995).

[27] T. Akylas and R. Grimshaw, J. Fluid Mech. **242**, 279 (1992). An interesting feature in this particular case is that it consists of a single figure based on the earlier experimental work of D. Farmer and J. Smith, Deep-Sea Res. 27. 239 (1980), which was provided to T. Akylas and R. Grimshaw by Dr. Farmer.

[28] G. Iooss, G. James, Chaos **15**, 015113 (2005).

[29] J.P. Boyd, Nonlinearity **3**, 177 (1990).

[30] N. Lu, J. Diff. Eqs. **256**, 745 (2014).

[31] J. Boyd, *Weakly nonlocal solitary waves and beyond-all-orders asymptotics*, Kluwer (Amsterdam, 1998).

[32] J.P. Boyd, Acta Applicandae **56**, 1 (1999).

[33] B.S. Lazarov, J.S. Jensen, J. Nonlin. Mech. **42**, 1186 (2007).

[34] P.G. Kevrekidis, A. Vainchtein, M. Serra-Garcia, Phys. Rev. E **87**, 042911 (2013).

[35] L. Bonanomi, G. Theocharis, C. Daraio, arXiv:1403.1052.

[36] G. Gantzounis, M. Serra-Garcia, K. Homma, J.M. Mendoza, C. Daraio, J. Appl. Phys. **114**, 093514 (2013).

[37] K. Vorotnikov, Y. Starosvetsky, G. Theocharis, P.G. Kevrekidis, preprint, submitted to Phys. D (2013).

[38] T. Kawahara, J. Phys. Soc. Jpn **33**, 260 (1972); see also: C.I. Christov, G.A. Maugin, M.G. Velarde, Phys. Rev. E **54**, 3621 (1996).

[39] E. B. Herbold and V. F. Nesterenko, Phys. Rev. Lett. **110**, 144101 (2013).

arXiv:1411.7062v1 [cond-mat.other] 25 Nov 2014

SUPPLEMENTAL MATERIAL:
Highly Nonlinear Wave Propagation in Elastic Woodpile Periodic Structures

E. Kim,[1] F. Li,[1] C. Chong,[2] G. Theocharis,[3] J. Yang,[1] and P.G. Kevrekidis[2]

[1]*Aeronautics and Astronautics, University of Washington, Seattle, WA 98195-2400*
[2]*Department of Mathematics and Statistics, University of Massachusetts, Amherst MA 01003-4515, USA*
[3]*Laboratoire d' Acoustique de l' Université du Maine, UMR-CNRS, 6613 Avenue Olivier Messiaen, 72085 Le Mans, France*

(Dated: November 27, 2014)

PACS numbers: 45.70.-n 05.45.-a 46.40.Cd

EXPERIMENTAL SETUP.

Figure 5 shows digital images of the experimental woodpile setup constructed in this study. The chain is supported by vertically-standing guiding rods, which constrain the horizontal, in-plane motions of the cylindrical elements and prevent buckling of the chain. To align the rods along the chain in parallel, we position soft polyurethane foam (firmness: 4.1 - 6.2 kPa under 25% deflection) between the tips of the rods. We find that the effect of the supporting foam on the cylinders' motions during wave propagation is negligible, because of the orders-of-magnitude lower stiffness of the foams compared to the rigidity of the cylinders or the contact stiffness of the vertically stacked cylindrical rods. As a result, we clearly observe the nanopteron tails with the Laser Doppler vibrometer despite that the amplitude of the vibration is extremely small in the order of tens of nm.

PARAMETER DETERMINATION FOR DEM.

For the construction of the DEM, we need to determine the parameters of a unit cell in terms of its discretized mass and spring coefficients (e.g., M, m_1, and k_1 as shown in the boxed region of Fig 1 (b)). In this study, these parameters are calculated via an optimization process based on the finite element method (FEM) (details are described in the reference [15] of the main manuscript). For example, Fig. 6(a) shows the temporal profiles of numerically simulated contact forces in the case of a 40 mm woodpile granular crystal. From the FEM result, it is evident that this locally resonating structure develops a modulated shape of propagating waves, which is in agreement with the experimental results as presented in Fig. 2(b). For the optimization process, we extract the overall shape of the modulated waveform by taking the maximum values of overlapped contact force (see red markers in Fig. 6(a)). The next step involves tuning the parameters of the DEM to match this baseline curve obtained by the FEM. For this, we begin

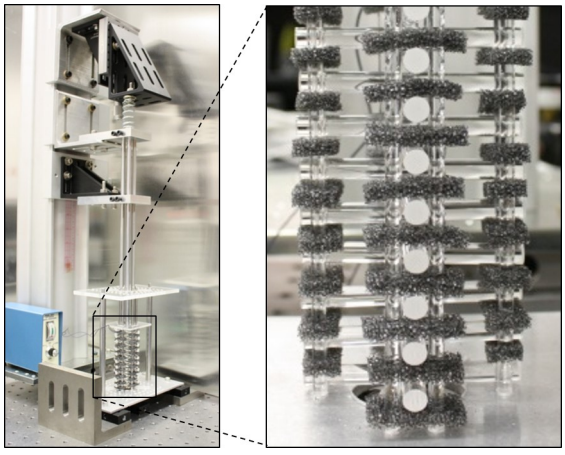

FIG. 5: Experimental setup of a woodpile granular crystal composed of orthogonally stacked 40 mm rods. A magnified view is shown on the right.

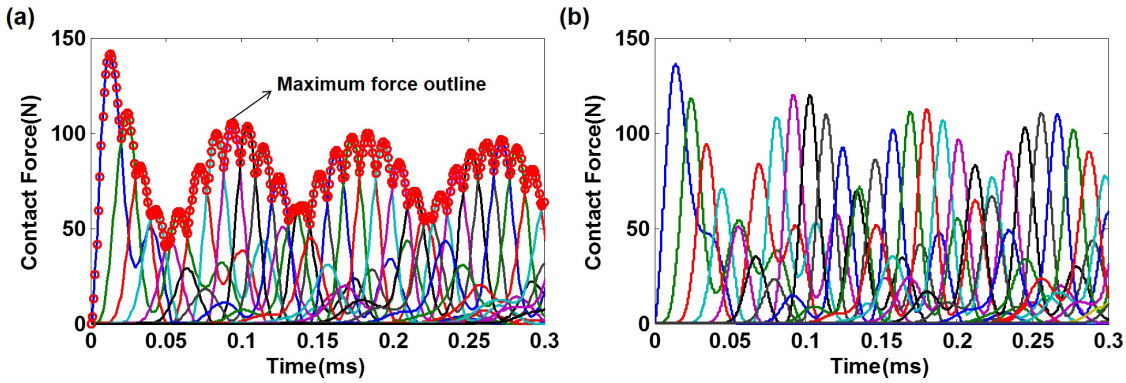

FIG. 6: Contact force profiles for a 40 mm woodpile granular crystal from (a) FEM simulation and (b) DEM simulation with optimized parameters.

TABLE I: Discretized mass distribution and spring coefficients in woodpile granular crystals.

Rod length	Total mass (g)	M (g)	m_1 (g)	m_2 (g)	k_1 (kN/m)	k_2 (kN/m)
20 mm	0.866	0.423	0.443	-	26267	-
40 mm	1.732	0.838	0.894	-	3961	-
80 mm	3.464	1.00	1.80	0.664	532	6423

with an initial mass distribution, M and m_1, and compute the stiffness of k_1 based on $\omega_0 = \sqrt{\kappa(1+1/\nu)}$, where $\kappa = k_1/\beta_c$ and $\nu = m/M$. Note that ω_0 is a resonant frequency of the unit cell (i.e., 40 mm rod) calculated from the FEM, and β_c is given simply by the Hertzian contact law. Based on these mass and stiffness values, we simulate the wave propagation via the DEM and obtain the modulated waveforms as shown in Fig. 6(b). We then compare it with the baseline data and iterate this process until we get optimized parameters that yield the best match between the FEM and the DEM. The optimized parameters for discretized masses and spring coefficients are summarized in Table I for woodpile granular chains with rod lengths of 20, 40, and 80 mm. Note, from all the possible internal vibration modes of the rods, only the symmetric bending modes are relevant to the dynamics due to symmetry considerations [1].

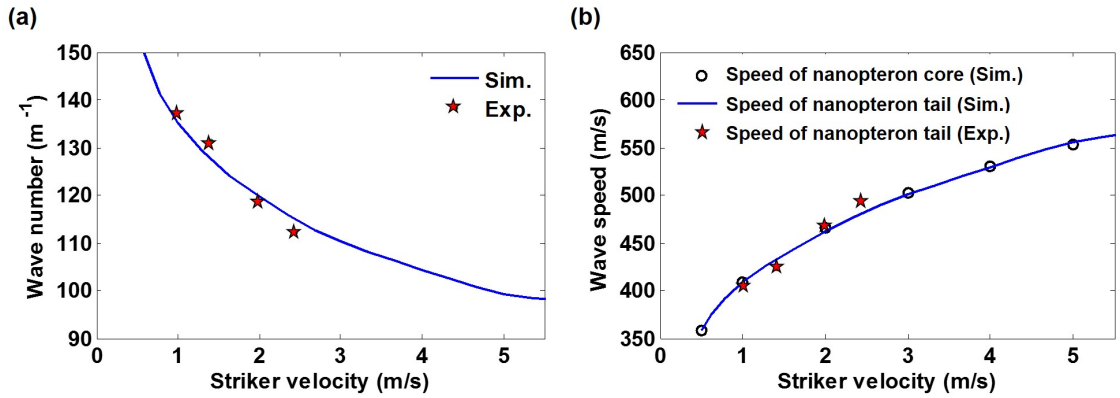

FIG. 7: (a) Wavenumber and (b) speed of sonic vacuum nanopteronic (SVN) tails (i.e., wings) as a function of various striker velocities (20 mm rods). Blue curves denote DEM results, while the start markers are experiment data measured from four different striker velocities: [0.99 1.40 1.97 2.42] m/s. The wave speed is also calculated alternatively by tracing the solitary waves (i.e., core part of the nanopteron) as marked by hollow circles.

EFFECT OF STRIKER VELOCITY VARIATION.

The speed of solitary waves in a discrete chain connected with Hertzian-type contact depends on the wave amplitude, i.e., $c \propto F_m^{1/6}$ where F_m is the force magnitude of propagating waves. This force magnitude is strongly dependent on striker velocity [2]. Thus, it can be interpreted that the speed of nanopteron (i.e., both of the solitary wave part and tail) increases as we impose a higher striker velocity on the woodpile granular crystal. This is because the wave speed of the nanopteronic tail is the same as the speed of the core, namely $c = \omega_0/k_0$, where ω_0 and k_0 are the frequency and wavenumber of the nanopteronic, respectively. We numerically verify this using the chain composed of 20 mm rods under various striker velocities (Fig. 7). Specifically, we first compute velocity profiles of all particles in the chain using the DEM. Based on the velocity profiles of the nanopteronic tails, we obtain wavenumbers and frequencies by conducting FFT in the space- and time-domain, respectively. The wavenumber varies as a function of striker velocity as shown in Fig. 7(a), while the extracted frequencies coincide with the natural frequency of the cylindrical elements. The wave speed is obtained directly from ω_0/k_0 (blue curve in Fig. 7(b)). This is in agreement with the speed of the core part of the nanopteron (i.e., solitary waves' speed) as marked by hollow circles in Fig. 7(b). Experimental results corroborate the numerical simulations by the DEM (star markers in Fig. 7).

SEMI-ANALYTICAL DESCRIPTION OF WAVE PROPAGATION

In the absence of the local resonators, Eq. (1) possesses exact traveling wave solutions [3–5]. Two classical approaches to obtain an analytical approximation to the evolution of the traveling wave in the presence of perturbations are the map approach [6] and the binary collision approximation (BCA) [7]. In this section, we amend these two methods in order to study the traveling waves in the presence of the local resonators. It should be noted here that the map approach presented below in the presence of resonators was already developed in the work of [8], whose discussion we adapt for our present comparison with the experimental results.

A Map Approach

Ignoring the boundary effects (i.e. considering an infinite chain), we write the equations of motion in terms of the strain variables $r_i = u_{i-1} - u_i$ and $s_i = v_{i-1} - v_i$

$$\ddot{r}_i = [r_{i-1}]_+^{3/2} - 2[r_i]_+^{3/2} - [r_{i+1}]_+^{3/2} + \kappa(s_i - r_i), \tag{8}$$

$$\ddot{s}_i + \omega^2 s_i = \omega^2 r_i \tag{9}$$

where $\omega^2 = \omega_0^2 - \kappa = \kappa/\nu$. Viewing the right hand side of Eq. (9) as an inhomogeneity suggests expressing the solution in terms of the Green's function of the operator $[\frac{d^2}{dt^2} + \omega^2]$

$$s_i(t) = \omega \int_{-\infty}^{t} \sin(\omega(t-\tau)) r_i(\tau) d\tau.$$

Substituting this expression into Eq. (8) yields

$$\ddot{r}_i = [r_{i-1}]_+^{3/2} - 2[r_i]_+^{3/2} + [r_{i+1}]_+^{3/2} + \kappa \left(\omega \int_{-\infty}^{t} \sin(\omega(t-\tau)) r_i(\tau) d\tau \right) - \kappa r_i. \tag{10}$$

In the absence of the local resonators ($\kappa = 0$), it is well known that Eq. (10) possesses solitary wave solutions [3–5]. One of the earlier results of Nesterenko relates the amplitude A of the traveling wave to its velocity [9]

$$r_i(t) = A \cdot S(A^{1/4} t - i)$$

where $S(\xi)$ is the profile of the wave. While there are several analytical approximations of this profile, based on e.g. a long wavelength approximation [9–11], we use the one recently developed in [11], which has the form

$$S(\xi) = \left(\frac{1}{q_0 + q_2 \xi^2 + q_4 \xi^4 + q_6 \xi^6 + q_8 \xi^8} \right)^2 \tag{11}$$

where $q_0 \approx 0.8357$,$q_2 \approx 0.3669$, $q_4 \approx 0.0831$, $q_6 \approx 0.0125$ and $q_8 \approx 0.0011$. If we assume that traveling wave form is maintained in the presence of the local resonators, but has a possibility decaying amplitude, then we have

$$r_i(t) = A_i S(A_i^{1/4} t - i), \tag{12}$$

where S is given by Eq. (11). Substituting this expression into Eq. (10) yields

$$A_i^{3/2} S_i'' = [A_{i-1}S_{i-1}]_+^{3/2} - 2[A_i S_i]_+^{3/2} + [A_{i+1}S_{i+1}]_+^{3/2} + \kappa A_i \left(\omega \int_{-\infty}^{t} \sin(\omega(t-\tau)) S(A_i^{1/4}\tau - i) d\tau \right) - \kappa A_i S_i \tag{13}$$

where we used the notation $S_i = S(A_i^{1/4} t - i)$. Since the peak of the traveling wave occurs for $T_i = i A_i^{-1/4}$, and the tail of the solutions asymptotes monotonically to zero, we can write Eq. (13) as a discrete map by integrating from $(-\infty, T_i)$

$$\begin{aligned} 0 = \quad & A_{i-1}^{3/2} \int_{-\infty}^{T_i} S^{3/2}(A_{i-1}^{1/4} t + i - 1) dt - 2A_i^{3/2} \int_{-\infty}^{T_i} S^{3/2}(A_i^{1/4} t + i) dt + A_{i+1}^{3/2} \int_{-\infty}^{T_i} S^{3/2}(A_{i+1}^{1/4} t + i + 1) dt \\ & + \kappa A_i \left(\omega \int_{-\infty}^{T_i} \int_{-\infty}^{t} \sin(\omega(t-\tau)) S(A_i^{1/4}\tau - i) d\tau \, dt \right) - \kappa A_i \int_{-\infty}^{T_i} S(A_i^{1/4} t + i) dt \end{aligned}$$

where we assumed $A_i > 0$ and $S_i > 0$. Several of the integrals appearing in this expression can be evaluated after a change the variable $t \to A^{1/4} t + i$. Thus we define

$$\begin{aligned} f_1 &= \int_{-\infty}^{0} S^{3/2}(t-1)\, dt \approx 2.5051, \\ f_2 &= \int_{-\infty}^{0} S^{3/2}(t)\, dt \approx 1.3215, \\ f_3 &= \int_{-\infty}^{0} S^{3/2}(t+1)\, dt \approx 0.1379, \\ g &= \int_{-\infty}^{0} S(t)\, dt \approx 1.2551 \end{aligned}$$

such that

$$0 = \quad A_{i-1}^{5/4} f_1 - 2A_i^{5/4} f_2 + A_{i+1}^{5/4} f_3 + \kappa A_i \left(\omega \int_{-\infty}^{T_i} \int_{-\infty}^{t} \sin(\omega(t-\tau)) S(A_i^{1/4}\tau - i) d\tau \, dt \right) - \kappa A_i^{3/4} g.$$

Assuming that local resonators create small perturbations of size ϵ such that $A_{i-1} = A_i + \mathcal{O}(\epsilon)$ finally yields a one dimensional discrete map

$$A_{i+1} = \left(\frac{A_i^{5/4} f_1 + \kappa A_i \left(\omega \int_{-\infty}^{T_i} \int_{-\infty}^{t} \sin(\omega(t-\tau)) S(A_i^{1/4}\tau - i) d\tau \, dt \right) - \kappa A_i^{3/4} g}{2f_2 - f_3} \right)^{4/5}. \tag{14}$$

By construction, the arrival time at the ith lattice site will be $T_i = i A_i^{-1/4} + \phi_0$, where ϕ_0 is used to calibrate the position of the first peak. To check the validity of this approximation, we compare the approximate decay of the peaks and corresponding arrival times to the DEM simulations. In Fig. 8 we consider the parameter values determined by the optimization procedure described in Table I for a rod length of 40 mm. In this case, the arrival time and strain value r of the initial traveling wave front compare favorably among the experiment, full DEM calculation, and map based on Eq. (14).

In the main text, three types of behavior are observed based on rod length, namely (i) the spontaneous formation (and steady propagation) of the nanopteron (found in the 20mm rod), (ii) the potential breathing of the traveling solitary waves (in the 40mm rod) or (iii) the decay of the solitary waves (in the 80mm rod) without relying on internal damping. This is due to the fact that each rod length yields different values of the resonant frequency. Thus, varying the resonant frequency will allow one to observe behavior ranging from modulated waves (i.e., breathing) to sonic-vacuum-nanoptera. For example, Fig. 9 compares simulations of the DEM model and the map (Eq. (14)) for other

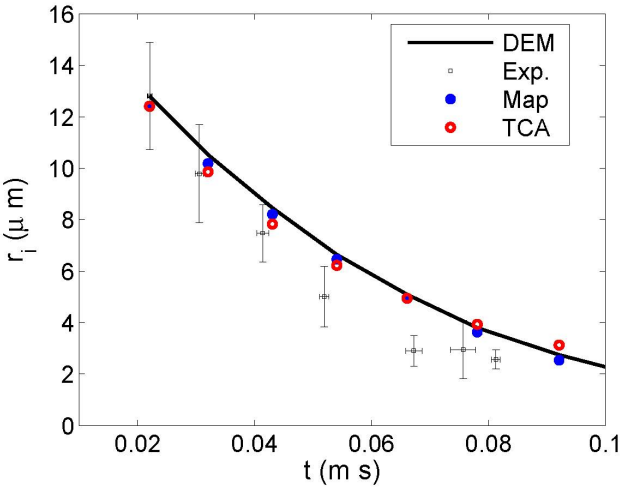

FIG. 8: Arrival times and corresponding strains r_i of the initial traveling wave front in the 40 mm rod set up as predicted by the DEM simulation (black line), the discrete map (blue points) and the TCA (red circles). The squares with error bars are the experimentally measured values, where the standard deviations were computed using five experimental runs.

values of the local resonant frequency κ, while keeping the other parameter values fixed. The modulation effect, which is due to the presence of secondary waves, is not captured by the map approach, which only takes into account the effects of the initial wave. Smaller values of the parameter κ correspond to slower decay of the initial traveling wave front, which is captured well by the map approach. Likewise, as κ is increased, the decay rate increases. However, in the full DEM model, the secondary wave effects have an immediate impact, which the map approach fails to predict, see Fig 9(c) and (d). In panel (d), one sees the development of the nanopteron. Note that the role of the secondary wave in numerical observations was also discussed in [8]. In Figs. 8 and 9 the predictions based on a ternary collision approximation (TCA) are also shown, which is detailed in the following section.

An Extension of the BCA: A Ternary Collision Approximation

The main purpose of the binary collision approximation (BCA) is to offer an approximation of the solitary wave velocity, or rather, the arrival time of the pulse for a given bead. The idea is to solve a simplified set of equations over a time scale where the dominant effects are between two adjacent beads only. In some cases, the resulting simplified equations can be solved exactly, the solution of which can be used to initialize the following step. Stringing the approximations together yields an approximation over the desired time span.

Employing the same procedure for the DEM model, Eqs. (1) and (2) in the main manuscript leads to a ternary collision approximation (since two primary masses and a local resonator are now involved). The simplified equations in the rescaled variables have the form

$$\begin{aligned} \ddot{u}_0 &= [u_0 - u_1]_+^{3/2} - \kappa(u_0 - v), \\ \ddot{u}_1 &= [u_0 - u_1]_+^{3/2}, \\ \ddot{v} &= \omega^2(u_0 - v). \end{aligned}$$

where u_0 is the displacement of the impacted bead, u_1 is the displacement of the bead adjacent to it, and v is the displacement of the local resonator of the impacted bead. Now define $r = u_0 - u_1$ and $s = u_0 - v$. We have then

$$\begin{aligned} \ddot{r} &= -2[r]_+^{3/2} - \kappa s, \\ \ddot{s} &= -[r]_+^{3/2} - \left(\kappa + \omega^2\right) s. \end{aligned} \tag{15}$$

The goal is to use these equations to obtain an approximation for the arrival time of the pulse. Recall that the arrival time at the ith site corresponds to the time where $r_i(t)$ obtains its first local maximum, or equivalently when the velocities of the adjacent beads become equal, since by definition $r_i = u_{i-1} - u_i$. For the first iteration, we use

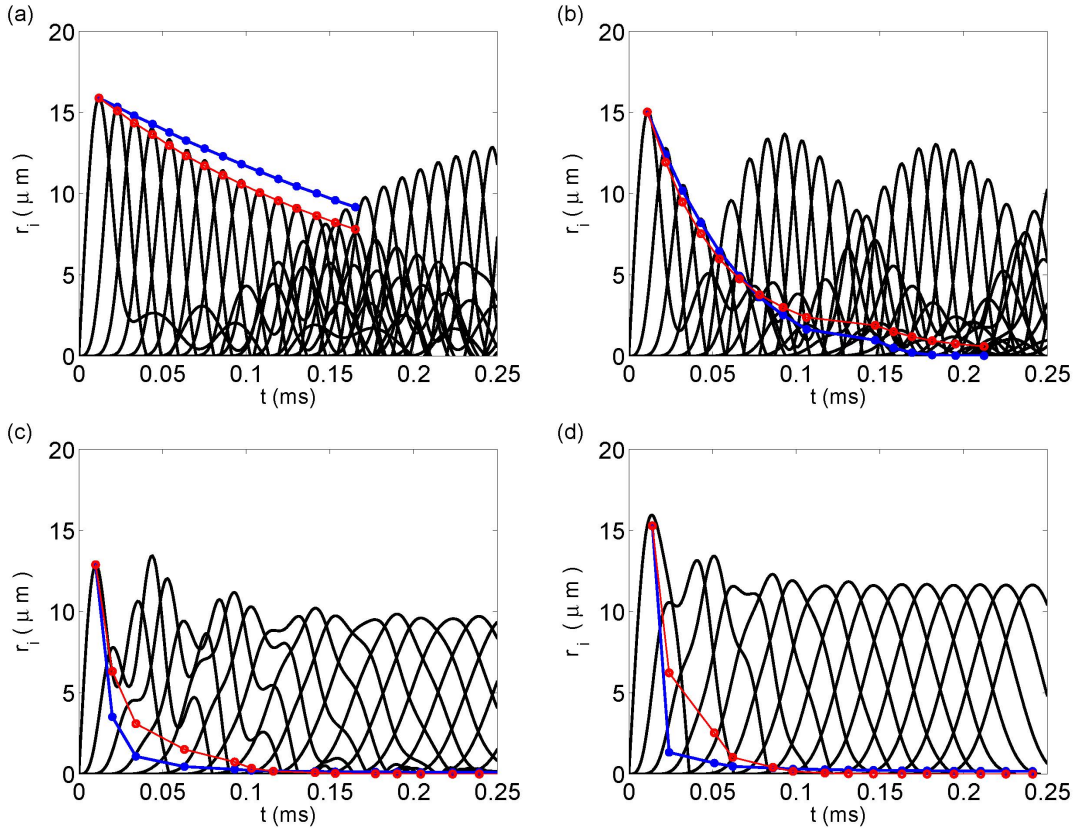

FIG. 9: Plot of the strain r_i for beads $i = 1, \ldots, 15$ from the full DEM simulation (black lines) and the decay of the peaks as predicted by the map approach (blue points) and the TCA (red circles). All parameter values correspond to those determined by the optimization procedure described in Table I with the exception of the resonant frequency k_1 (kN/M), which has the value (a) $k_1 = 788$, (b) $k_1 = 3961$, (c) $k_1 = 15760$, and (d) $k_1 = 23641$. The resonant frequency of panel (b), $k_1 = 3961$, corresponds to the value in Table I for the 40mm rod. Due to the immediate effect of the secondary waves in the higher frequency cases shown in panels (c-d), both the map approach and TCA are inaccurate. In panel (d) one can see how the core part of the nanopteronic forms. The tail part, however, cannot be discerned at this resolution.

the initial value $r(0) = s(0) = 0$ and $\dot{r}(0) = \dot{s}(0) = V_0$, where V_0 is the velocity of the striker bead. Upon solving system (15), we define the first arrival time t_1 such that $\dot{r}(t_1) = 0$. For the subsequent iterations, we use the initial value $r(0) = s(0) = 0$ and $\dot{r}(0) = \dot{s}(0) = V_i$. In the absence of the local resonator, the traveling wave does not decay, and hence $V_i = V_0$. We assume however, that resonator will indeed cause the peak to decay. We estimate the decay based on the first iteration. Namely, we define

$$V_i = V_0\, a^{i-1}, \qquad a = \frac{\dot{r}(t_1;\kappa)}{\dot{r}(t_1;0)}$$

where $r(t_1;0)$ is the solution of (15) at time $t = t_1$ with the resonator parameter $\kappa = 0$ and $r(t_1;\kappa)$ is the solution of (15) at time $t = t_1$ with the resonator parameter $\kappa \neq 0$. In other words, a is the decay between the first and second peak, and we assume the decay rate remains constant. Since the TCA is an iterative procedure, the ith arrival time t_i is based on an initial time of $t = 0$. Thus, the actual arrival time at site i is $T_i = \sum_n^i t_n$. The pulse arrival times based on the TCA using the parameter values corresponding to the 40 mm rod are shown as the red circles in Fig. 8, where we found $a \approx 0.8$. This method also compares favorably to the experiment, full DEM simulation and the map approach. To estimate the amplitude of peak i, we used the formula $A_0 a^i$, where A_0 is the amplitude of the first peak computed from the DEM. These predictions are shown as red circles in Fig. 9.

Here, the TCA reduced an infinite dimensional system of ODEs into a system of two second order equations (see e.g. Eq. (15)). However, the simplified system does not lend itself to a closed form analytical solution, and thus we resorted to numerical simulations of Eq. (15). Nonetheless, the favorable agreement between the TCA and full DEM simulations demonstrates that the predominant features of the initial traveling wave front at a given time are adequately captured by the simplified model bearing two primary masses and a local resonator.

[1] E. Kim and J. Yang, J. Mech. Phys. Solids **71**, 33 (2014).
[2] C.Coste, E. Falcon, and S. Fauve, Phys. Rev. E **56**, 6104 (1997).
[3] G. Friesecke and JAD Wattis, Commun. Math Phys. **161**, 391 (1994).
[4] J.M. English and R.L. Pego, Proceedings of the AMS **133**, 1763 (2005).
[5] A. Stefanov and P.G. Kevrekidis, J. Nonlinear Sci. **22**, 327 (2012).
[6] Y. Starosvetsky, Phys. Rev. E **85**, 051306 (2012).
[7] K. Lindenberg, U. Harbola, H. Romero, and A. Rosas. Pulse Propagation in Granular Chains. *American Institute of Physics Conference Series* **1339**, 97–110 (2011).
[8] K. Vorotnikov, Y. Starosvetsky, G. Theocharis, P.G. Kevrekidis, preprint, submitted to Phys. D (2013).
[9] V.F. Nesterenko, *Dynamics of Heterogeneous Materials*. Springer-Verlag, New York (2001).
[10] K. Ahnert and A. Pikovsky, Phys. Rev. E **79**, 026209 (2009).
[11] Y. Starosvetsky, A.F. Vakakis, Phys. Rev. E **82**, 026603 (2010).